Enhancing the CO 2 -to-CO Conversion from 2D Silver Nanoprisms via Superstructure Assembly

Kun Qi, Yang Zhang, Ji Li, Christophe Charmette, Michel Ramonda, Xiaoqiang Cui, Ying Wang, Yupeng Zhang, Huali Wu, Wensen Wang, et al.

Enhancing the CO_2-To-CO Conversion From 2D Silver Nanoprisms *via* Superstructure Assembly

*Kun Qi[1‡], Yang Zhang[1,2‡], Ji Li[3], Christophe Charmette[1], Michel Ramonda[4], Xiaoqiang Cui[5], Ying Wang[5], Yupeng Zhang[6], Huali Wu[1], Wensen Wang[1], Damien Voiry[1]**

[1] Institut Européen des Membranes, IEM, UMR 5635, Université Montpellier, ENSCM, CNRS, Montpellier 34000, France

[2] Institute of Microscale Optoelectronics, Shenzhen University, Shenzhen 518060, China

[3] College of Bioresources Chemical and Materials Engineering, Shaanxi University of Science and Technology, Xi'an 710021, China

[4] Central Technology in Micro and Nanoelectronics CTM-LMCP, Université Montpellier, Montpellier 34000, France

[5] State Key Laboratory of Automotive Simulation and Control, Department of Materials Science, Key Laboratory of Automobile Materials of MOE, Jilin University, Changchun 130012, China

[6] Key Laboratory of Optoelectronic Devices and Systems of Ministry of Education and Guangdong Province, College of Electronic Science and Technology, Shenzhen University, Shenzhen 518060, China

ABSTRACT.

The electrochemical reduction of CO_2 in a highly selective and efficient manner is a crucial step towards its reuse for the production of chemicals and fuels. Nanostructured Ag catalysts have been found to be effective candidates for the conversion of CO_2 to CO. However, the ambiguous determination of the intrinsic CO_2 activity and the maximization of the density of exposed active sites has greatly limited the use of Ag towards the realization of practical electrocatalytic devices. Here, we report a superstructure design strategy prepared by the self-assembly of two-dimensional Ag nanoprisms for maximizing the exposure of active edge ribs. The vertically stacked Ag nanoprisms allow exposure of > 95% of the edge sites, resulting in an enhanced selectivity and activity towards the production of CO from CO_2 with an overpotential of 152 mV. The Ag superstructures also demonstrates a selectivity over 90% for 100 hours together with a current retention of ≈ 94% at -600 mV *versus* the reversible hydrogen electrode and a partial energy efficiency for CO production of 70.5%. Our electrochemical measurements on individual Ag nanoprisms with various edge-to-basal plane ratios and the Ag superstructures led to the identification of the edge ribs as the active sites thanks to the ≈ 400 mV decrease in the onset potential compared to that of the Ag (111) basal planes and a turnover frequency of $9.2 \times 10^{-3} \pm 1.9 \times 10^{-3}$ s^{-1} at 0 V overpotential.

KEYWORDS. silver, two-dimensional materials, self-assembly, CO_2 reduction reaction, electrocatalysis

Introduction

The fast increasing atmospheric carbon dioxide (CO_2) concentration is a critical challenge for human society.[1] The CO_2 electrochemical reduction reaction using electrical energy generated from renewable sources hold promises for the production of useful chemical species, such as carbon monoxide (CO), formic acid, methanol, ethylene or methane.[2,3] The high overpotentials and the relative low selectivity of the electrocatalysts toward the formation of specific products currently hamper the development of this reaction into economically-viable technology. These challenges partially originate from the parasite hydrogen evolution reaction (HER) in aqueous electrolytes, the low concertation of dissolved CO_2 in the electrolyte and the inadequate crystal facets regulation of the catalysts.[4-6] Among the various products of the CO_2 reduction reaction (CO_2RR), CO can be obtained from CO_2 with selectivity approaching 90%.[7-9] The electrochemical reduction of CO_2 to CO follows a two-electron reduction pathway: $CO_2 + 2H^+ + 2e^- = CO + H_2O$ with a relatively low standard redox potential of -110 mV *versus* the reversible hydrogen electrode (RHE).[10,11] Hydrogen (H_2) and CO can advantageously be used as synthetic gas (syngas) for producing chemicals *via* the Fischer-Tropsch process.[12] Ideal electrocatalyst for CO_2RR is expected to deliver large current densities and maintain a high selectivity and stability toward the desired reduction products.[13,14] To meet these criteria, both optimal surface binding energies of CO_2 and the reaction intermediates and fast electron transfer between reaction intermediates and the catalyst surface must be achieved. Silver (Ag) has been identified as a promising candidate for the CO_2-to-CO reaction thanks to the moderate binding of the key reaction intermediate *COOH and the weak binding energy of *CO, which favors rapid release for the product of the reaction.[15,16] Recent studies have shown that the performance of Ag-based electrocatalysts can be significantly improved by tailoring the nanostructures and the surface chemical compositions.[17,18] In this

context, crystal engineering has provided insight into the influence of the surface of catalyst for the CO_2RR activity and selectivity.[19] Strategies based on alloying, downsizing and controlling the geometry of the Ag crystals have been proposed for preferably exposing specific crystal facets and therefore enhancing the CO_2RR activity.[20-22] For example, the catalytic activity has been shown to follow a volcano-shaped trend for CO_2RR with respect to the size of the Ag nanocrystals.[23] Alternatively, the change in the dimensionality of the Ag nanostructures from 0D to 2D results in the improvement of the performance towards the production of CO thanks to the reduced binding energy for the *COOH intermediate.[24] Although these contributions have opened new directions for engineering nanostructured Ag for CO_2RR, the Faradaic efficiency and intrinsic activity such as the turnover frequencies (TOFs) have remained challenging to be precisely estimated – making it impossible to fairly compare the Ag-based catalysts' CO_2RR performance with other electrocatalysts. More importantly, strategies for maximizing the exposure of the active sites are still lacking; preventing further developments of Ag-based electrodes for the selective conversion of the CO_2 and water into syngas.

Here, we report a procedure to preferentially expose the edge sites of two-dimensional Ag nanoprisms (2D Ag-NPs) *via* the preparation of superstructures (denoted as 2D Ag-SS) using the self-assembly method. Our density functional theory (DFT) calculations are used as the guidance indicate that the edge ribs and the corner sites of 2D Ag-NPs possess a reduced energy barrier for the proton-coupled electron transfer (PCET) associated with the formation of the *COOH intermediate thanks to higher local electron density. By controlling the strong van der Waals interactions between the basal plane of the nanoprisms, we demonstrate the successful vertical stacking of the 2D Ag-NPs. Specifically, we show that the structure of the 2D Ag-SS preferentially exposes the Ag edges of the nanoprisms up to > 95% in agreement with our numerical predictions

and therefore maximizes the exposure of the active edge ribs and corner sites. Once vertically assembled, the 2D Ag-SS exhibit strongly enhanced activity compared to that of the pristine 2D Ag-NPs with a reduced onset potential of only 152 mV *vs.* RHE, a carbon monoxide Faradaic efficiency (FE_{CO}) of 96.3% and a partial energy efficiency for CO production (EE_{CO}) of 70.5% at -600 mV *vs.* RHE along with excellent long-term stability with negligible changes of the CO_2RR current density and FE_{CO} over 100 hours. To elucidate the origin of the activity from the edge ribs, we examined the catalytic properties of the 2D Ag-NPs with various edge-to-basal plane ratios and we estimated that the TOFs reach $\approx 458 \pm 58\ s^{-1}$ at -600 mV *vs.* RHE that is over 100-fold larger than the best reported Ag-based electrocatalyst.

Results and discussion

Theoretical and statistical predictions of the CO_2RR activity from 2D Ag nanoprisms:

To rationalize the design of the 2D Ag-NPs and identify the CO_2RR active sites, we first scrutinized the Gibbs free energy (ΔG) for the evolution of CO on silver nanostructures. For a better understanding of the different sites of 2D Ag-NPs, the top and side views of the atomic structures of a typical Ag nanoprism are presented in **Figure 1a** and **1b**. The basal plane is dominated by Ag (111) facet, whereas the edges are typically dominated by Ag (100).[25] Two peculiar sites can also be identified: the edge ribs and the corner sites of the nanoprisms whose atomic structure significantly differs from that of Ag (111) and Ag (100) due to local crystal twinning of the atomic structure. The electrochemical reduction reaction of CO_2 on the electrode surface is known to involve key intermediate species such as *COOH and *CO to produce CO or *CHO and *COH for the production of methane and methanol respectively. Previous numerical simulations have shown that the appropriate binding energy of *COOH relative to that of *CO translates into improved activity and the overall reaction rate.[26] The Gibbs free energies for the

reaction from the different Ag facets: Ag (111) and Ag (100) together with the edge ribs and corner sites are presented in **Figure 1c**. In all the cases, the largest energy barrier is associated with the formation of *COOH and corresponds to the thermodynamically limiting step. This first PCET step therefore dictates the thermodynamic overpotential of the reaction.[24] The required ΔG to form the *COOH on Ag edge ribs and corner sites is significantly lower than on Ag (100) and Ag (111), suggesting improved thermodynamic characteristics at the edge ribs and corner sites towards CO_2RR.[27] The binding energy of CO_2 was also found to be virtually identical for Ag (111), Ag (100), Ag rib and Ag corner sites (Supplementary Figure XX). To further confirm the influence on the catalytic performance of *COOH as the key intermediate species, we evaluated the binding energy of *COOH as a function of the binding energy of *CO. As illustrated in **Figure 1d**, the Ag (111), Ag (100) and the corner sites exhibit an obvious linear scaling relation between the binding energies of *COOH and *CO.[28-30] Such a scaling severely limits the minimum achievable overpotential for the reduction of CO_2. Breaking the linear scaling by decreasing the binding energy of *COOH while keeping that of *CO constant is desirable to improve the activity and the associated turnover frequency. Such an approach has recently been proposed using gold nanowires.[31] Our numerical predictions indicate that the edge ribs can better stabilize *COOH over *CO suggesting that they do not strictly obey the scaling relation between the two intermediate species – making the edge ribs promising toward the CO_2-to-CO conversion reaction.

To understand the origin of the binding energy on Ag, we calculated the local charge density of each individual site (inset Figure 1d). The greater electron accumulation (shown in yellow) suggests an increase in the density of valence electrons from the Ag atoms connected to *COOH, possibly due to the local electron transfer from the surrounding Ag atoms. In addition, the higher charge density can also be responsible for the faster electron transfer and the increase of the binding

energy between Ag and adsorbed *COOH.[32] Compared to the Ag (111) and Ag (100) facets, the improved adsorption of *COOH on the edge ribs and corner sites is expected to involve more valence electrons connected with *COOH and thus to accelerate the CO_2RR kinetics while facilitating the thermodynamics. Our results on the adsorption energy and the local charge density at the active sites thus revealed that both the edge ribs and the corner sites of 2D Ag-NPs are the preferred active sites for the CO_2-to-CO conversion on Ag and call for the development of strategies for maximizing the edge exposure of 2D Ag-NPs to improve the catalytic performance of nanostructured Ag catalysts.

Structure engineering of the metal catalyst has been the recent focus of investigations in the field of electrocatalysis in order to optimize the density of active sites at the surface of the electrodes for the HER, the oxygen evolution reaction (OER) and especially for the electrochemical reduction of CO_2. Different atomic surface structures – *i.e.* crystal facets – of a metal catalyst may have different electronic configurations and coordination environments, resulting in different catalytic properties.[33,34] To illustrate the influence of the morphology of the silver nanoparticles on the density of active sites, we computed the evolution of the edge ribs and corners sites with the size of various nanoparticles for two-dimensional prismatic, octahedral and cubic geometries. The relationship between the active site ratio and size is illustrated in **Figure 1e** for different morphologies of Ag nanoparticles. Compared with the Ag nanocubes – dominated by Ag (100) facets – and the Ag nanooctahedral – dominated by Ag (111) facets – the Ag nanoprisms exhibit larger ratios. Downsizing of the silver nanoparticles has been proposed to increase the density of active sites – often at the cost of the selectivity and the ease of preparation – but offers a limited perspective towards practical use for the CO_2 conversion.[35] Conversely, increasing the size of the nanoprisms would lead to the rapid increase of the catalytic inert basal plane and result in a lower

density of edge ribs and corners sites. Similar considerations have previously been discussed in the case of other edge-active nanomaterials.[36] As shown in Figure 1e, the exposed active sites will be limited to ≈ 50% if only adjusting the morphology and downsizing the nanocrystals – thus fundamentally restricting the density of exposed active sites.[24] Alternatively, vertical stacking of the 2D nanoprisms can advantageously be used to further increase the density of active edge ribs without compromising the edge-to-basal plane ratio. As shown in **Figure 1f**, the stacking of the nanoprisms in the superstructure leads to a rapid increase of the edge-to-basal plane ratio up to nearly 100% when the number of nanoprisms in the superstructure is greater than 200. From our numerical simulations, we hypothesized that vertical stacking of the 2D Ag-NPs can enhance the catalytic performance of Ag catalysts by maximizing the density of active sites.

Fabrication of Ag nanoprisms superstructure on the substrate:

To address the potential of the 2D Ag superstructures made of vertically stacked nanoprisms, we prepared 2D Ag-NPs with different sizes using a seed-mediated growth method.[37] The size of the 2D Ag-NPs was tuned in order to vary the edge-to-basal plane ratio by controlling the amount of injected Ag seed into the colloidal suspension (See the Methods section for details about the synthesis). Transmission electron microscopy (TEM) was used to assess the homogeneity and particle size statistics for the different 2D Ag-NPs (**Figure 2a-2c**). Our observations revealed that the crystals consist of two-dimensional triangular shape nanoprisms without the discernible presence of other types of morphology and the lateral dimension of the nanoprisms can vary from 40 nm up to over 1 μm. TEM and atomic force microscopy (AFM) measured were used to provide statistics on the average edge length and thickness of the 2D Ag-NPs. The average edge length was estimated to be 1050 nm ± 31 nm, 510 nm ± 22 nm and 52 nm ± 6 nm with a corresponding thickness of 17 nm ± 2.8 nm, 12 nm ± 1.5 nm and 10 nm ± 0.9 nm for the large, medium and small

2D Ag-NPs, respectively (**Figure 2d and 2e**). The self-assembly of the nanoprisms was achieved *via* the control of the van der Waals interactions between the 2D materials.[38] The interactions between the 2D Ag-NPs were obtained by capping the monodispersed 2D Ag-NPs with sodium citrate on the surface.[39,40] The assembly process occurs spontaneously after drop-casting of the 2D Ag-NPs ink on the surface of the supporting electrode followed by the controlled evaporation of the solvent (See the Methods section for details). The vertical stacking of the 2D Ag-NPs was further confirmed by X-ray diffraction (XRD) measurements. As shown in **Figure 2f**, pristine 2D Ag-NPs exhibit an intense diffraction peak from the (111) lattice plane at $2\theta = 38.12°$ together with a weak peak at $2\theta = 44.30°$ which belongs to the (200) planes of fcc Ag (JCPDS No. 04-0783). In the case of the 2D Ag-SS, a different pattern is observed with a strong contribution from the (200) peak together with a weak (111) peak. This clearly points out that the (100) plane from the edges is the main exposed facet for the 2D Ag-SS compared to (111), which further indicates that the 2D Ag-NPs are vertically stacked along their basal planes in the case of the 2D Ag-SS and the (111) planes from the edges of the nanoprisms are preferentially oriented perpendicular to the supporting substrate in perfect agreement with our TEM and high-resolution transmission electron microscopy (HRTEM) observations presented in **Figure 2g**. Prior to assessing the CO_2RR activity from the 2D Ag-SS, the excess of organic ligand was removed by electrochemical cleaning methods (See the Methods section for details). After the cleaning process, the individual 2D Ag-NPs are clearly visible from the 2D Ag-SS whereas no obvious changes on the morphology or the stacking can be detected from the TEM observations (**Figure 2h**).[41] We also compared the X-ray photoelectron spectroscopy (XPS) spectrum on the 2D Ag-SS before and after the electrochemical cleaning process to confirm the efficient removal of the organic capping agent (**Figure 2i, Supplementary Figure 1**). Again, minimal change was detected from the surface of Ag according

to the Ag 3d XPS spectrum, while the C=O bonding disappeared from the C1s region; confirming that the successful removal of the organic ligand without changing the surface oxidation state of silver.[42]

CO_2RR activity and stability measurement:

The CO_2RR electrocatalytic activity was evaluated using an H-type cell in a standard three-electrode configuration and the loading amount for each Ag catalyst was kept constant at 0.5 mg cm^{-2} (See the Methods section for details).[43] **Figure 3a** presents the linear sweep voltammetry (LSV) curves recorded both in argon (Ar) (dot line) and CO_2 (solid line) saturated 0.1 M KOH (see the Method section for details) for the different sizes of 2D Ag-NPs and the 2D Ag-SS. The increase of the current density in the Ar-saturated electrolyte is ascribed to the reduction of protons to form H_2. When Ar is replaced with CO_2, the current density increases concurrently with a positive shift of the onset potential, implying the occurrence of CO_2 reduction.[44] By comparing the LSV curves in Ar- and CO_2- saturated electrolyte, we observed an obvious increase of the current density in CO_2 – hinting at the high selectivity towards the reduction of CO_2 from the 2D Ag-SS. Interestingly the LSV responses of Ag-NPs and Ag-SS are virtually identical in Ar-saturated electrolyte, whereas Ag-SS exhibits clearly higher current densities in CO_2-saturated conditions – suggesting a possible faster reaction rates for CO_2RR compared to HER. The vertical alignment of the nanoprisms on the electrode support in the case of the Ag-SS is also expected to improve the charge transfer and charge transport to the active sites as observed previously on the case of other 2D materials. We also found that the current density at a given potential continuously increases with the decrease of the size of the 2D Ag-NPs. At -600 mV *vs.* RHE, the smallest 2D Ag-NPs shows the highest current density 1.7 mA cm_{Geom}^{-2} (normalized by the geometrical surface of the electrode). At the same potential, the current density from the 2D Ag-SS prepared with the

same size of 2D Ag-NPs increases ≈ 2.5-fold to 4.19 mA cm_{Geom}^{-2}. The onset potential for 2D Ag-SS extracted from the LSV curves is also estimated to 152 mV *vs.* RHE, which corresponds to a 246 mV positive shift compared with that from the 2D Ag-NP counterparts, and 52 mV lower than for previous reports on 2D Ag-NPs.[24]

To further confirm the CO_2 reduction performance, we carried out steady-state chronoamperometric measurements at different potentials between -300 and -900 mV *vs.* RHE (**Supplementary Figure 2**). The products were analyzed by ^1H nuclear magnetic resonance spectroscopy and gas chromatography.[45] As shown in **Figure 3b**, CO and H_2 were the only products in the gas phase and no liquid product was detected. For all the potentials, we observed a rapid increase of the Faradaic efficiency for CO (FE_{CO}) as the size of the 2D Ag-NPs decreases. FE_{CO} of the 2D Ag-SS is also found to be significantly higher than that of the different 2D Ag-NPs over the full potential range and peaks at 96.3 % for the 2D Ag-SS catalyst at -600 mV *vs.* RHE. At the same potential, the FE_{CO} for small, medium and large 2D Ag-NPs reaches 65.4 %, 51.05% and 50.01% respectively. The partial energy efficiency for CO production for the 2D Ag-SS is estimated to be 70.5% at -600 mV *vs.* RHE, which is one of the highest values ever reported for the conversion of CO_2 to CO (**Supplementary Table 2**). We determined the electrochemically active surface area (ECSA) and the roughness factor using the lead (Pb) under potential deposition method and the measurement of the double layer capacitance respectively (See the Methods section). **Figure 3c** compares the partial current density for CO production (j_{CO}) of different catalysts normalized by electrochemically active surface area (ECSA) ((**Supplementary Figure 3, 4** for details about the ECSA measurements). $j_{CO\ ECSA}$ increases with the decrease of the lateral dimension of 2D Ag-NPs strongly supporting the fact that the increased edge-to-basal plane ratio directly translates into larger CO_2-to-CO activity and lower hydrogen production. More

importantly, the partial current density for CO is strongly enhanced in the case of 2D Ag-SS with a $j_{\mathrm{CO\ ECSA}}$ = -3.5 mA cm_{ECSA}^{-2} at -600 mV *vs.* RHE and compares favorably with the best results from the literature (**Supplementary Table 3**). Finally, we investigated the stability of the 2D Ag-SS catalysts over 100 hours at the optimal potential of -600 mV *vs.* RHE (**Figure 3d**). The current was continuously measured while the gas products were injected into the gas chromatograph every 4 hours. The performance from the 2D Ag-SS is found very stable with almost constant cathode current density and minimal drop of FE_{CO}. After 100 hours, the retention of the current density and the FE_{CO} reach 92.5% and 95%, respectively. To further confirm that this performance is not affected by any potential degradation of the electrode surface, we estimated the roughness factor (RF) of the electrode before and after a 100-hours operation. Our cyclic voltammetry measurements indicate that the RF change from 3.75 to 3.52 – corresponding to a 93.8 % retention confirming that the active sites are retained after the long term stability measurement without any dissolution of the Ag-SS catalysts (**Supplementary Figure 5**).[46] The surface state of the catalysts was further characterized after the stability measurement and negligible oxidation is detected from the Ag 3d XPS spectrum, while TEM observations revealed no obvious change of the morphology of the superstructures (**Supplementary Figure 6**). Taken together, the electrochemical investigations of 2D Ag-SS validate our strategy of edge engineering of the 2D Ag nanoprisms *via* self-assembly into vertical superstructures.

Investigations of the CO_2RR enhancement mechanism:

To gain insight into the origin of the enhancement of the CO_2RR activity, we examined the relationship between FE_{CO} / FE_{H2} and the edge-to-basal plane ratio of the different electrodes. **Figures 4a and 4b** represent the evolution of the Faradaic efficiency for the two gas products at -300, -600 and -900 mV *vs.* RHE with the percentage of edge-to-basal plane ratio obtained from

the TEM and AFM measurements (**Supplementary Table 4**). For clarity, the other potentials are plotted in **Supplementary Figure 7 and 8** and show the same tendency. We first observe that, at the same applied potential, there is an obvious linear relationship between the FE for both CO and H_2 and the edge-to-basal plane ratio. The positive slope observed for the evolution of FE_{CO} suggests that the selectivity towards the CO evolution increases together with the edge exposure. Conversely, the negative slope in the case of FE_{H2} indicates that the selectivity towards H_2 is inversely proportional to the presence of the edge sites. We also note that the largest slope – indicating the stricter relationship between the Ag edges and the FE_{CO} – is obtained at -600 mV *vs.* RHE in a qualitative agreement with the trend observed in Figure 4b. **Figure 4c and 4d** show the partial current density for CO and H_2 based on the current densities and the corresponding FE for the different edge-to-basal plane ratios. For each potential, j_{CO} rapidly increases with the edge-to-basal plane ratio, while j_{H2} remains virtually constant or even decreases at -600 mV or -700 mV *vs.* RHE, which are the most effective potentials for CO_2RR. Our electrochemical measurements demonstrate that the CO_2RR performance is strictly controlled by the density of exposed edges of the 2D Ag-NPs. By fitting the evolution of j_{CO} and j_{H2} for the different edge-to-basal plane ratios, we extrapolated the theoretical partial current density at 0% edges sites – *i.e*. in absence of edges – whereas the partial current density at 100% edges – *i.e.* in absence of basal plane – was extracted from the values of the 2D Ag-SS. As illustrated in **Figure 5a**, our results show that j_{CO} for 0% edge sites remains negligible at potentials lower than ≈ -700 mV *vs.* RHE suggesting the Ag (111) from the basal planes can only reduce CO_2 into CO with a large overpotential of ≈ 590 mV *vs.* RHE. Conversely, in the case of 100% edge sites (**Figure 5b**), j_{CO} rapidly starts increasing from ≈ -300 mV *vs.* RHE – equivalent to a minimal overpotential of ≈ 190 mV. Such a large reduction of

the onset potential unambiguously confirms the improved thermodynamics for the reduction of CO_2 on the edge ribs and corner sites.

The exchange current density (i_0) reflects the intrinsic rate of the electron transfer between the electrolyte and the electrode, thus provide qualitative information on the binding energy of the reaction intermediates and a high value of i_0 traditionally reflects improved thermodynamics for the reaction.[47] The exchange current density was extracted from the FE_{CO}-normalized polarization curves for the different sizes of 2D Ag-NPs and the 2D Ag-SS.[48] Interestingly, our results show that the exchange current density linearly increases with the percentage of edge-to-basal plane ratio as expected for the edges being the main active site of the reaction (**Figure 5c**).[49] A final evidence supporting the edges being the active sites was brought by the controlled deactivation of the edges of the nanoprisms. Because the edges have larger surface energy, they are more prone to be oxidized or etched.[50] The edges of the 2D Ag-NPs were controllably converted to Ag_2O by mixing the suspension of the 2D Ag-NPs with 10 M KOH at room temperature.[51] After 2 days, the oxidation of the edges was confirmed by our TEM and HRTEM observations and the oxidized edges appear as dark regions on the triangles, while the formation of Ag_2O was further identified from the SAED pattern (**Figure 5d and Supplementary Figure 9**). Direct observation of the edge oxidation was also brought by the EDS mapping and the EDS line scan of the of the oxidized Ag nanoprisms (Figure 5e-g, Supplementary Figure10). The electrocatalytic behavior of the oxidized Ag NPs was then recorded using the same conditions as for the pristine counterparts. Our results revealed that after oxidation, both the current density and the FE_{CO} are strongly suppressed translating into a partial current density $j_{CO\ ECSA}$ of only 0.026 mA cm^{-2} at -600 mV *vs.* RHE compared to 1.28 mA cm^{-2} in the case of pristine 2D Ag-NPs (**Figure 5e**). On the contrary, the partial current density for hydrogen is largely preserved in agreement with the (111) basal planes

being more HER active. To avoid any influence of the aggregation of the Ag nanoprisms on the CO_2RR properties, we also performed the oxidation of the edge sites of Ag-SS after fabricating the electrode. As shown in **Supplementary Figure 10**, by comparing the LSV curves of Ag-SS and oxidized Ag-SS (Ag_2O-SS), an obvious decrease of the current density was observed after the oxidation of the edge sites suggesting a low selectivity towards the reduction of CO_2 from the Ag basal plane. The deactivation of the Ag superstructures was further confirmed by the strong decrease of the FE_{CO} in the case of edge-oxidized Ag-SS. This induces a strong decrease in the partial current density j_{CO} and j_{H2} in the case of Ag_2O-SS and j_{CO} for the Ag_2O-SS is only -0.005 mA cm^{-2} at -600 mV *vs.* RHE compared to -1.94 mA cm^{-2} in the case of pristine Ag-SS. Ag_2O is expected to be reduced upon decreasing the potential at the working electrode since the standard potential $E^{\circ}_{Ag_2O/Ag}$ is +342 mV *vs.* SHE. The reduction of the oxidized edge is however unlikely to restore the structure of the pristine edges of the nanoprisms and therefore the CO_2RR properties should remain poor. To confirm our hypothesis, the activity of oxidized Ag-SS (Ag_2O-SS) was gauged after cycling for 1 hour and we found no obvious change of the performance (**Supplementary Figure 11**). This result demonstrates that the formation of Ag_2O at the edge ribs permanently suppresses the CO_2RR activity. Taken together, our experimental and DFT results point out the role of the edge ribs of the 2D Ag-NPs as the active sites for the CO_2-to-CO reaction.[48,52]

Estimation of the intrinsic activity from the edge sites:

To further assess the intrinsic activity from the edge sites of the 2D Ag-NPs, we prepared electrodes consisting of individual 2D Ag-NPs. The different sizes of 2D Ag-NPs were deposited on mechanically polished glassy carbon using spin coating and the conditions of deposition were optimized in order to have isolated nanoprisms on the electrode surface (See the Methods section

for details). The density of 2D Ag-NPs, as well as the total edge length and basal plane surface per cm^2 of electrodes were statistically analyzed using AFM. **Figures 6a-6c** show the AFM images of the 3 different sizes of 2D Ag-NPs loaded on the surface of the glassy carbon electrode. The edge ribs and corners of every individual 2D Ag-NPs are indicated by the white lines as shown in **Figure 6d-6f**. According to the AFM analyses over ≈ 500 μm^2, the electrode coverage for the large, medium and small 2D Ag-NPs on the glassy carbon electrodes was estimated to 2.84 ± 0.42%, 3.06 ± 0.54 % and 2.92 ± 0.31 % respectively (**Supplementary Figure 12**). We also estimated the area of edge sites per geometrical area (nm^2/nm^2_{geom}) of GC electrodes from the total edge lengths and the thickness of the different 2D Ag-NPs (**Supplementary Table 4**). The TOF values were then estimated assuming the active sites are coming from the edge ribs and corners alone and using the values of FE_{CO} presented in Figure 3b. The TOFs values for the 2D Ag-NPs were further compared with other reports from the literature (**Figure 6g**).[53-65] We found that the TOF values from the Ag edges do not significantly vary between the different sizes of 2D Ag-NPs in agreement with the (111) basal planes being non-active for the reaction. The average TOFs from the nanoprisms reaches 458 ± 58 s^{-1} at -600 mV *vs.* RHE that is over 100-fold larger than the best reported Ag-based electrocatalyst from the literature. We also estimated the TOFs from exchange current density and found the TOF at $\eta = 0$ V reaches $9.2 \times 10^{-3} \pm 1.9 \times 10^{-3}$ s^{-1}.

Conclusions

In summary, we report a strategy for vertically stacking two-dimensional Ag nanoprisms into highly active superstructures *via* a self-assembly method. The rational design of the superstructures allows to preferentially expose mostly the active edge ribs and corner sites of the 2D Ag-NPs. The vertically stacked 2D Ag superstructures with a large edge-to-basal plane ratio exhibits outstanding electrocatalytic activity for CO_2RR with a high CO Faradaic efficiency of 96.3% and partial energy

efficiency of 70.5% at -600 mV *vs.* RHE and excellent long-term stability with negligible CO_2RR current density and CO Faradaic efficiency change for 100 hours. The precise control of the superstructure designs led to the identification of the edge ribs as the active sites for the CO_2-to-CO reaction in perfect agreement with our numerical simulations. By combining physical characterizations and electrochemical measurements, we determined the overpotential for CO evolution from the edge ribs and the basal planes to be ≈ 190 mV and ≈ 590 mV respectively. The strategy described here highlights the opportunity for fine-tuning the structure and the functionality of metal catalysts at the atomic scale and holds promise for applications in large-scale carbon fixation and energy conversation electrolysers.

Methods

Preparation of Ag nanoprism nanoseeds.

Ag nanoprism seed solution was synthesized by a modified chemical reduction method. In a typical synthesis, 12 mL of 0.075M trisodium citrate dihydrate ($HOC(COONa)(CH_2COONa)_2 \cdot 2H_2O$, ACS reagent, Sigma Aldrich), 200 μL of 0.1 M silver nitrate ($AgNO_3$, ACS reagent, Sigma Aldrich) and 480 μL of hydrogen peroxide solution (H_2O_2, ACS reagent, 30wt.%, Sigma Aldrich) were dissolved in 200 mL of H_2O. After that, 1.2 mL of 0.1 M freshly-prepared sodium borohydride solution ($NaBH_4$, ≥98%, Sigma Aldrich) was added by quick injection under vigorous stirring, giving rise to a blue solution of Ag nanoprism seeds, which was then used as a stock solution.

Preparation of Ag nanoprisms with different sizes.

In a typical synthesis of 2D Ag nanoprisms (2D Ag-NPs), 5 mL of acetonitrile (CH_3CN, 99.8%, Sigma Aldrich), 150 μL of 0.1 M L-ascorbic acid ($C_6H_8O_6$, ACS reagent, Sigma Aldrich), 100 μL of 0.075M trisodium citrate dihydrate were added together in 10 mL of H_2O at 5°C. An aliquot of

the stock solution was centrifuged, and the Ag nanoseeds were redispersed in H_2O of one-fifth of the original volume just before the serve as the seed solution. Under vigorous stirring, the acetonitrile solution was mixed with the appropriate volume of the seed solution added, followed by the injection of 120 μL of 0.1 M silver nitrate to initiate the seeded growth. The reaction was allowed to proceed under stirring at 5°C for 30 min, followed by centrifugation for collecting. The lateral dimensions of the 2D Ag-NPs were controlled by adjusting the volume of the seed solution. Specifically, the volumes of the seed solution were adjusted to 12 mL, 2 mL and 200 μL for the synthesis of 2D Ag-NPs with the average size of 52 nm, 510 nm and 1100 nm, respectively. A prolonged reaction time up to 30 min was necessary to complete 2D Ag-NPs growth when a large size is targeted.

Preparation of 2D Ag superstructures.

In a typical synthesis of 2D Ag superstructures (2D Ag-SS), the smallest size of 2D Ag-NPs with lateral dimensions of 52 nm was typically used. 2mL of as-prepared 2D Ag-NPs were dissolved in 2 mL 0.1 M trisodium citrate dihydrate solution. After 5 mins sonication, the solution with a typical concentration of 0.12 mg mL^{-1} was drop cast on the mechanically polished glassy carbon electrode. Then the electrode was stored in the humid environment to allow slow evaporation of the solvent. The electrodes with the vertically-oriented 2D Ag-NPs were finally stored in the vacuum.

Characterizations.

Transmission electron microscopy images (TEM) were obtained using a JEOL 1400 microscope with an emission gun operating at 120 kV. HRTEM images were obtained using HRTEM JEOL 2200 FS microscope with an emission gun operating at 200 kV. The samples for TEM and HRTEM were prepared by dropping ethanol dispersions of the samples onto 300 mesh carbon-coated copper

grids and then evaporating the solvent. Fast Fourier transform (FFT) masked contrast refined HRTEM images were obtained using Gatan digital micrograph software. AFM images were obtained in Digital Instruments Nanoscope IV in tapping mode with cantilevers with spring constant of 40 N/m and tip curvature < 10 nm and a frequency of 325 kHz. AFM was performed on the mechanism polished glass carbon electrode loaded with the materials by spinning coating. XPS measurement was performed using an ESCALAB-250 instrument (Thermo Fisher Scientific, USA), performed with a monochromatic Al-Kα (1486.6 eV) radiation source and a hemisphere detector with an energy resolution of 0.1 eV. Peak positions were all corrected by the C 1s spectrum at 284.8 eV. XRD measurement was performed on an Xpert Pro apparatus (Philips Pana Analytical, Cu Kα; λ = 1.5418 Å) operating at 40 kV and 20 mA. The scanning speed was set to 8° *per* min.

Electrochemical measurements.

The electrochemical measurements were performed using a mechanically polished glassy carbon electrode connected with a VSP potentiostat (Bio-Logic Science Instruments). The electrochemical cleaning process was performed by cyclic voltammetry scanning in 0.1 M KOH between 100 mV and -500 mV for 100 cycles with a scan rate of 50 mV s^{-1}. CO_2 reduction experiments were performed in a gastight two-compartment H type electrochemical cell separated by a piece of anion exchange membrane (Nafion-117). The electrolyte consisted in a 0.1 M KOH solution saturated with CO_2 with a pH value of 6.82. We found that after CO_2 saturation, the 0.1 M KOH solution is equivalent to a 0.1 M $KHCO_3$ solution (See Supplementary Figure 13 and further details in the Supplementary Information file). The "Ar-purged sample" in Figure 3a was acidified to pH ≈ 6.8 with CO_2 bubbling first, after that, the solution was re-saturated with the Ar. The final pH value was 8.26 against 8.30 in the case of the Ar-saturated 0.1 M $KHCO_3$ solution.

The working electrode (WE) was prepared by loading the catalyst ink (loading: 0.5 mg cm^{-2}) with the spinning coating method onto the mechanically polished glassy carbon electrode (2.5 cm x 2.5 cm). An Ag/AgCl (KCl saturated) electrode and platinum foil (3 cm x 3 cm) were used as the reference and counter electrodes, respectively. All potentials were calibrated to the reversible hydrogen electrode (RHE) by the equation:

$$E_{RHE} = E_{Ag/AgCl} + 0.059pH + 0.197 \qquad (1)$$

Linear sweep voltammetry (LSV) was conducted in Ar-saturated or CO_2-saturated 0.1 M $KHCO_3$ solution between 0 mV and -1000 mV *vs.* RHE to investigate the CO_2RR activity. A long-term stability test was recorded by taking a chronoamperometric curve at a constant potential of -600 mV *vs.* RHE. All data are presented without IR-compensation. All the electrochemical tests were performed at room temperature.

Preparation of the glassy carbon electrodes with isolated 2D Ag-NPs.

The isolated 2D Ag-NPs decorated glassy carbon electrodes were prepared by a spin coating process which includes four processes. First, 100 μL of concentrated 2D Ag-NPs colloid was drop cast in the centre of freshly mechanical polished glassy carbon electrode (2.5 cm x 2.5 cm). Then, 1000 rpm with an acceleration of 500 rpm s^{-1} was applied for 20 seconds to let the liquid spread all over the electrode. After that, the spin speed was decreased to 500 rpm with a deceleration of 200 rpm s^{-1} for 20 seconds to make the catalyst firmly attached to the surface of the electrode. Finally, the speed was increased to 3000 rpm for 30 seconds with an acceleration of 1000 rpm s^{-1} to dry the electrode and remove the excess of 2D Ag-NPs.

Estimation of the surface roughness factors.

The double-layer capacitance (C_{dl}) was used to estimate the surface roughness factors of the different Ag catalysts. The C_{dl} was measured by cycling the electrodes at increasing scan rates

from 10 mV s^{-1} up to 80 mV s^{-1} between 50 and 150 mV *vs.* RHE. The capacitance for the different electrodes was obtained from the slope of the difference of current density measured at 100 mV *vs.* RHE. The roughness factor was estimated by the ratio of the measured C_{dl} and the capacitance of Ag (25 μF cm^{-2}). The FE-normalized current densities per geometric area of the electrode were divided by the surface roughness factor to obtain the partial current densities ($j_{H_2\ ECSA}$ and $j_{CO\ ECSA}$).

Estimation of the ECSA via Pb under potential deposition (UPD).

Gas-phase product analysis.

Gas-phase product quantification was performed using an on-line gas chromatograph (Agilent, Micro GC-490) equipped with a TCD detector and Molsieve 5A column continuously. Hydrogen and Argon (99.999%) were used as the carrier gases. Gas-phase products were collected every 15 min using an automatic sampler to access catalyst selectivity and total partial current density. Gas quantification was based on prior calibration of the system injecting mixtures with a known percentage of gases.

Calculation of the partial energy efficiency.

The partial energy efficiency for CO production (EE_{CO}) of the catalysts was calculated using the following equation:

$$EE(\%) = \frac{\Delta E_0}{\Delta E_{applied}} \times FE \qquad (2)$$

Where ΔE_0 is the equilibrium full cell potential ($E_{CO_2/CO} - E_{water\ oxidation}$ = -0.11 V - 1.23 V = -1.34 V), $\Delta E_{applied}$ is the applied full cell potential ($E_{CO_2/CO\ (applied)} - E_{water\ oxidation}$ = -0.60 V - 1.23 V = -1.83 V), FE is the Faradaic efficiency for CO_2 convert to CO at -0.6 V *vs.* RHE.

Calculation of the turnover frequency.

The turnover frequencies (TOFs) was calculated by assuming that the basal plane sites not play a significant role in the CO_2RR performance and can be neglected (in this case, the highest TOFs is estimated) by the following equation:[54]

$$TOFs = \frac{jco}{C \times 1.2\times10^{15}\times R_{rib}\times 2e^{-}\times 1.6\times10^{-19}} \qquad (3)$$

here $j_{CO}(A.cm_{Geom}^{-2})$ is the measured current at a specific overpotential, C is the edge coverage of the electrode with the 2D Ag-NPs ($\frac{cm_{edge}^{-2}}{cm_{Geom}^{-2}}$), 1.2 × 10^{15} is the density of surface atoms for Ag (100) assuming an fcc structure with a lattice parameter of 4.09 Å.[66] R_{rib} ($\frac{n_{atom@ribs+corners}}{n_{atom@edges}}$) is the atomic ratio of the rib sites from the edges of the nanoprisms (See details in Supplementary Table 4).

DFT calculations.

All the density functional theory (DFT) calculations were implemented in the Vienna Ab-initio Simulation Package (VASP) code with a projector augmented-wave (PAW) method.[67,68] The exchange-correction energy was described using a generalized gradient approximation (GGA) with a Perdew–Burke–Ernzerhof (PBE) format.[69] A plane-wave basis with a kinetic energy cutoff of 450 eV was chosen to expand the electronic wave functions. Additional details of the calculations are provided in the Supplementary Information.

Images and figures

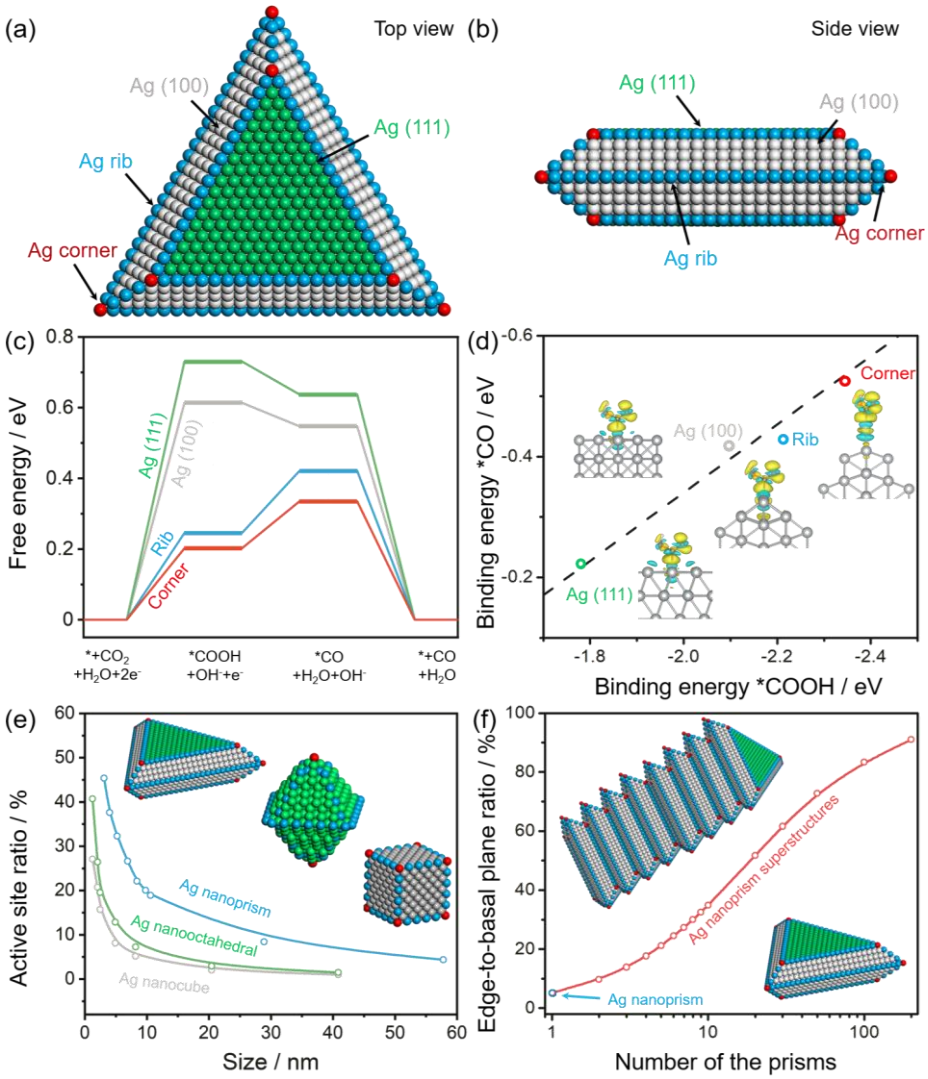

Figure 1. Theoretical calculation of CO_2 reduction reaction on the Ag nanoprims. a-b, Top and side view of the silver nanoprism, which shows the detailed facet information of the structure. **c**, Free energy diagrams for electrochemical reduction of CO_2 to CO of different Ag sites. **d**, Binding energies of the *COOH and *CO intermediates calculated on the Ag sites, inset shows the charge density iso-surfaces upon *COOH adsorption on the different Ag sites, yellow and blue contours represent electron accumulation and depletion, respectively. **e**, Active site ratio of three typical Ag structures (nanocube, nanooctahedral and nanoprism) with different sizes. **f**, Relationship between the edge-to-basal plane ratio and the number of assembled monomers. The lateral dimension of the nanoprims shown in the inset is 50 nm.

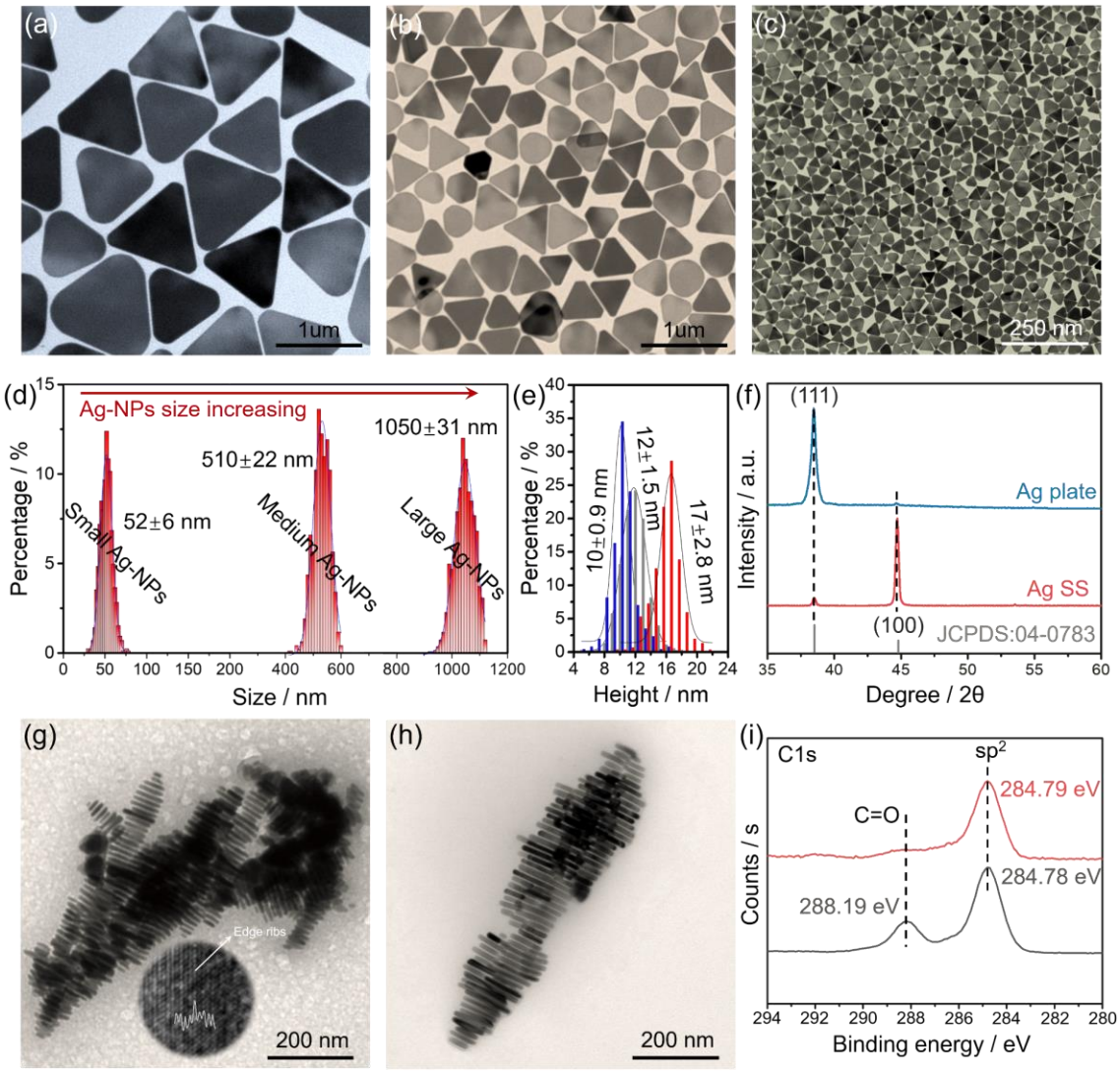

Figure 2. Characterization of different sizes of 2D Ag-NPs and the assembly of 2D Ag-SS. TEM images of the 2D Ag-NPs of different sizes. Ag seed colloid volumes are: **a**, 0.2 mL, **b**, 2 mL, **c**, 12 mL, respectively. **d**, Particle size statistical analysis for the different size 2D Ag-NPs. **e**, Particle height statistical analysis for the different size 2D Ag-NPs. **f**, XRD pattern of monodispersed 2D Ag-NPs and 2D Ag-SS. **g**, Typical lateral TEM image of the as-synthesized 2D Ag-SS, directly showing the cross-section structure of the 2D Ag-NPs. Inset shows the HRTEM image from the edge of a nanoprism. The position of the ribs can be identified from the average contrast. **h**, TEM image of 2D Ag-SS after electrochemical cleaning in 0.1 M KOH solution. **i**, C 1s XPS spectrum of 2D Ag-SS before (black) and after (red) the electrochemical cleaning process.

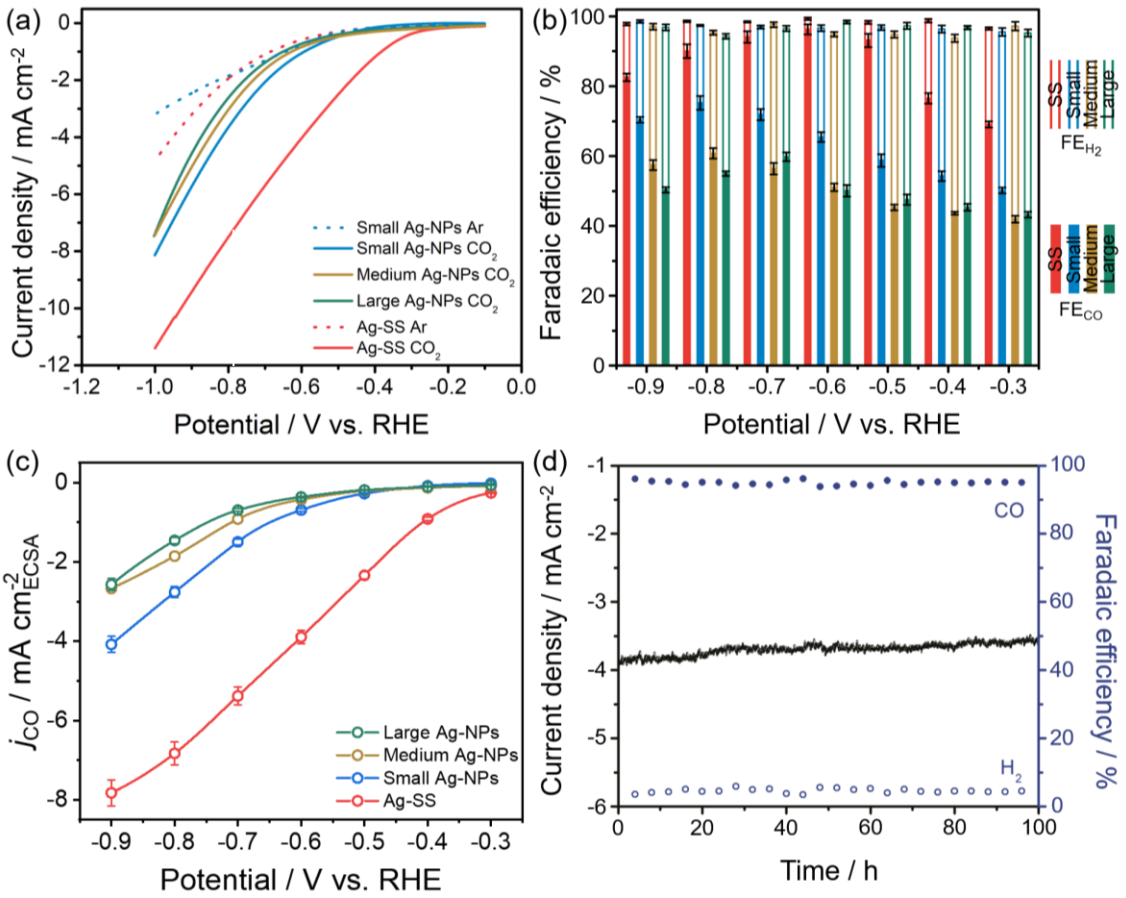

Figure 3. CO_2 electroreduction performance. **a**, CO_2 reduction cathodic linear sweep voltammetry (LSV) results of different catalysts. **b**, FE_{CO} and FE_{H_2} for different catalysts at various applied potentials. **c**, Partial current density for CO ($j_{CO\ ECSA}$) of different Ag catalysts normalized by the ECSA of different catalysts. **d,** Long-term stability measurement of 2D Ag-SS in CO_2-saturted 0.1 M KOH aqueous electrolyte under a CO_2 atmosphere (1 atm) at room temperature (25 °C) at -600 mV *vs.* RHE for 100 hours.

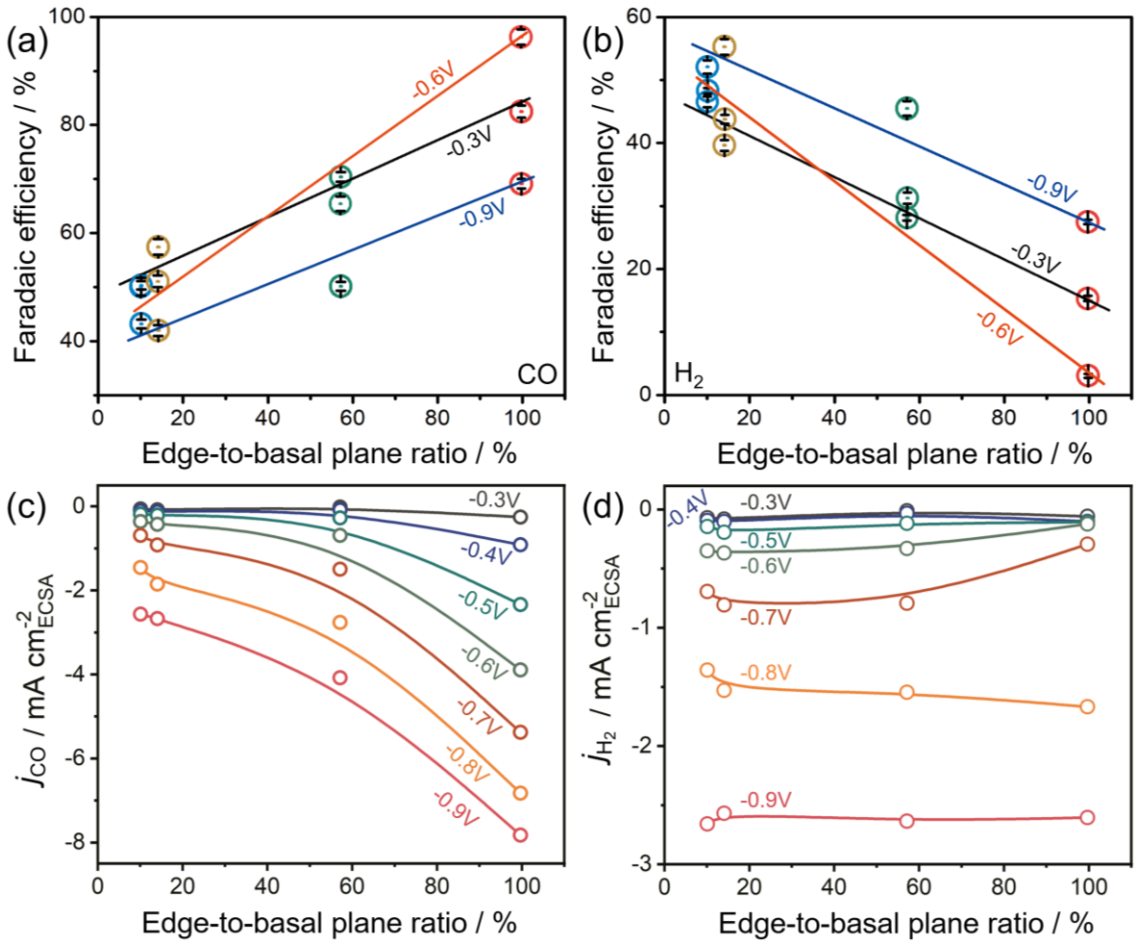

Figure 4. Electrochemical performance for CO_2 reduction electrolysis to CO and hydrogen evolution reaction on Ag structures. a, Relationship between the CO Faradaic efficiency (FE_{CO}) and different edge-to-basal plane ratio at various potentials. **b**, Relationship between the H_2 Faradaic efficiency (FE_{H_2}) and the different edge-to-basal plane ratio at various potentials. **c,** Partial CO current density (j_{CO}) at different edge-to-basal plane ratio and various applied potentials. **d**, Partial H_2 current density (j_{H_2}) at different edge-to-basal plane ratio and various applied potentials.

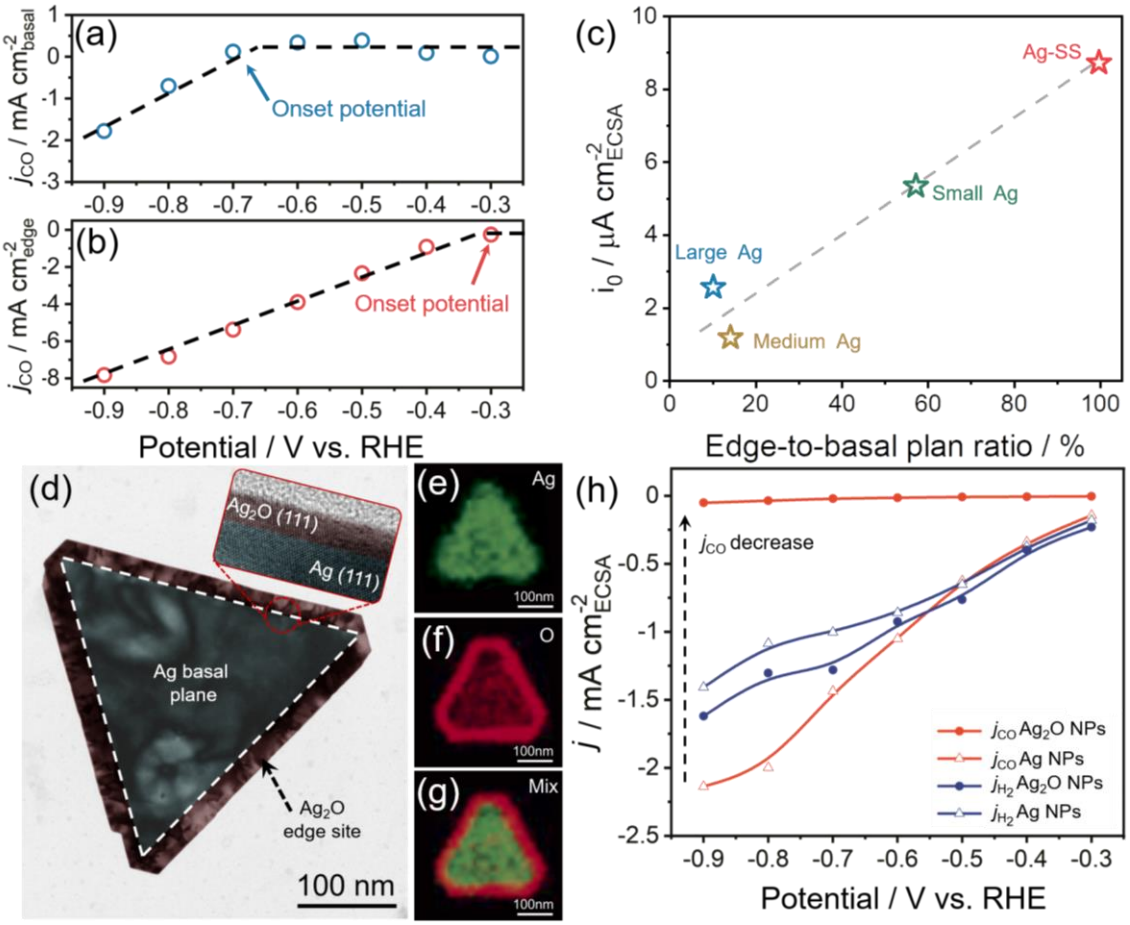

Figure 5. Confirmation of the edge as active sites for CO_2 electrochemical reduction to CO. **a**, Evolution of the j_{CO} from the basal plane with the applied potential. **b**, Evolution of the j_{CO} from the edge sites with the applied potential. **c**, Exchange current density (i_0) for different edge-to-basal plane ratios. **d**, Artificially colored TEM image of the edges of oxidized 2D Ag-NPs. Inset shows the HRTEM image of the oxidized edge. **e**, EDS elemental mapping of silver, **f,** oxygen and **g,** combined. The combined EDS mapping shows that the oxygen extends beyond the silver which informs the formation of an oxide layer on the edge site of Ag nanoprism while the basal plane was retained metallic. **h**, Partial current density of CO and H_2 for the pristine 2D Ag-NPs and edge-oxidized 2D Ag-NPs (Ag_2O-NPs).

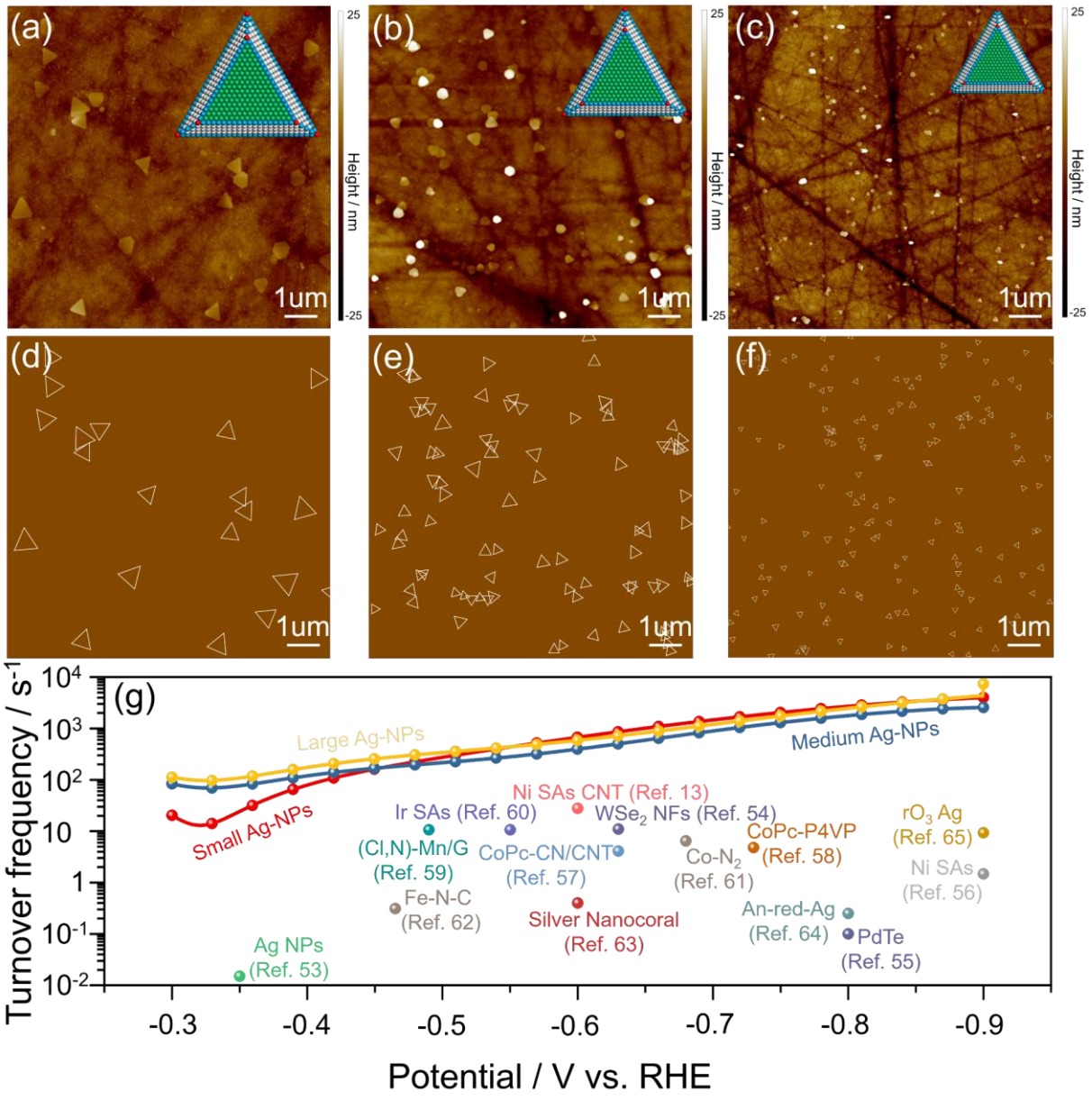

Figure 6. Characterization of the electrode decorated by different size 2D Ag-NPs and further CO_2RR active sites confirmation. a-c, AFM image of the glassy carbon electrode decorated with isolated 2D Ag-NPs. **d-f**, Corresponding computed images showing the edges of the nanoprisms. **g**, Evolution of the TOFs values from the edge sites (ribs + corners) from the 2D Ag-NPs of various sizes compared with other state-of-the-art CO_2 to CO reduction catalysts.

ASSOCIATED CONTENT

Supporting Information. The Supporting Information is available free of charge on the ACS Publications website at DOI:

Computational details, chronoamperometric curves, comparison of the partial energy efficiency, Pb UPD measurements, comparison of the CO_2RR performances, catalyst stability characterizations and AFM images (PDF)

AUTHOR INFORMATION

Corresponding Author

*E-mail: damien.voiry@umontpellier.fr (D. Voiry).

Author Contributions

D.V., K. Q. and Y. Z. designed and directed the research. K. Q., Y. Z., H. L. W., Y. P. Z and C. C. synthesized the materials and performed the materials property characterization. X. Q. C. and Y. W. performed the TEM characterization. M. R carried out the AFM characterization. J. L. and W. S. W. carried out and analyzed the theoretical results. K. Q. and D. V. wrote the manuscript. D. V. supervised the project and established the final version of the paper. All authors discussed the results and commented on the manuscript. All authors have approved the final version of the manuscript. ‡These authors contributed equally.

ACKNOWLEDGMENT

D. V., K. Q., H. W. acknowledge funding from the European Research Council (ERC) under the European Union's Horizon 2020 research and innovation programme (grant agreement No 804320). K. Q. and Y. Z. acknowledge financial support from the China Postdoctoral Science

Foundation (2018M633127) and Natural Science Foundation of Guangdong Province (2018A030310602).

Reference

1. Ren, S., Joulié, D., Salvatore, D., Torbensen, K., Wang, M., Robert, M. & Berlinguette, C. P. Molecular Electrocatalysts Can Mediate Fast, Selective CO_2 Reduction in a Flow Cell. *Science* **365**, 367-369 (2019).

2. Huang, J., Mensi, M., Oveisi, E., Mantella, V. & Buonsanti, R. Structural Sensitivities in Bimetallic Catalysts for Electrochemical CO_2 Reduction Revealed by Ag-Cu Nanodimers. *J. Am. Chem. Soc.* **141**, 2490-2499 (2019).

3. Huang, J., Hörmann, N., Oveisi, E., Loiudice, A., Luca De Gregorio, D., Andreussi, O., Marzari, N. & Buonsanti, R. Potential-Induced Nanoclustering of Metallic Catalysts during Electrochemical CO_2 Reduction. *Nat. Commun.* **9**, 1-9 (2018).

4. Rakowski Dubois, M. & Dubois, D. L. Development of Molecular Electrocatalysts for CO_2 Reduction and H_2 Production/Oxidation. *Acc. Chem. Res.* **42**, 1974-1982 (2009).

5. Zhou, K. & Li, Y. Catalysis Based on Nanocrystals with Well-Defined Facets. *Angew. Chem. Int. Ed.* **51**, 602-613 (2012).

6. Lee, H. E., Yang, K. D., Yoon, S. M., Ahn, H. Y., Lee, Y. Y., Chang, H. J., Jeong, D. H., Lee, Y. S., Kim, M. Y. & Nam, K. T. Concave Rhombic Dodecahedral Au Nanocatalyst with Multiple High-Index Facets for CO_2 Reduction. *ACS Nano* **9**, 8384-8393 (2015).

7. Franco, F., Rettenmaier, C., Jeon, H. S. & Cuenya, B. R. Transition Metal-Based Catalysts for the Electrochemical CO_2 Reduction: From Atoms and Molecules to Nanostructured Materials. *Chem. Soc. Rev.* **49**, 6884-6946 (2020).

8. Sa, Y. J., Lee, C. W., Lee, S. Y., Na, J., Lee, U. & Hwang, Y. J. Catalyst-Electrolyte Interface Chemistry for Electrochemical CO_2 Reduction. *Chem. Soc. Rev.* **49**, 6632-6665 (2020).

9. Zheng, T., Jiang, K., Ta, N., Hu, Y., Zeng, J., Liu, J. & Wang, H. Large-Scale and Highly Selective CO_2 Electrocatalytic Reduction on Nickel Single-Atom Catalyst. *Joule* **3**, 265-278 (2019).

10. Pegis, M. L., Roberts, J. A., Wasylenko, D. J., Mader, E. A., Appel, A. M. & Mayer, J. M. Standard Reduction Potentials for Oxygen and Carbon Dioxide Couples in Acetonitrile and N, N-Dimethylformamide. *Inorg. Chem.* **54**, 11883-11888 (2015).

11. Zheng, T., Jiang, K. & Wang, H. Recent Advances in Electrochemical CO_2-to-CO Conversion on Heterogeneous Catalysts. *Adv. Mater.* **30**, 1802066 (2018).

12. Dry, M. E. The Fischer-Tropsch Process: 1950-2000. *Catal. Today* **71**, 227-241 (2002).

13. Liu, S., Yang, H. B., Hung, S. S., Ding, J., Cai, W. Z., Liu, L. H., Gao, J. J., Li, X. N., Ren, X. Y., Kuang, Z. C., Huang, Y. Q., Zhang, T. & Liu, B. Elucidating the Electrocatalytic CO_2 Reduction Reaction over a Model Single-Atom Nickel Catalyst. *Angew. Chem. Int. Ed.* **59**, 798-803 (2019).

14. Voiry, D., Shin, H. S., Loh, K. P. & Chhowalla, M. Low-Dimensional Catalysts for Hydrogen Evolution and CO_2 Reduction. *Nat. Rev. Chem.* **2**, 0105 (2018).

15. Wei, L., Li, H., Chen, J. S., Yuan, Z. W., Huang, Q. W., Liao, X. Z., Henkelman, G. & Chen, Y. Thiocyanate Modified Silver Nanofoam for Efficient CO_2 Reduction to CO. *ACS Catal.* **10**, 1444-1453 (2019).

16. Sun, D., Xu, X., Qin, Y., Jiang, S. P. & Shao, Z. Rational Design of Ag-Based Catalysts for the Electrochemical CO_2 reduction to CO: A Review. *ChemSusChem* **13**, 39-58 (2020).

17. Lu, Q., Rosen, J., Zhou, Y., Hutchings, G. S., Kimmel, Y. C., Chen, J. G. & Jiao, F. A Selective and Efficient Electrocatalyst for Carbon Dioxide Reduction. *Nat. Commun.* **5**, 1-6 (2014).

18. Dutta, A., Morstein, C. E., Rahaman, M., Cedeño López, A. & Broekmann, P. Beyond Copper in CO_2 Electrolysis: Effective Hydrocarbon Production on Silver-Nanofoam Catalysts. *ACS Catal.* **8**, 8357-8368 (2018).

19. Tao, A. R., Habas, S. & Yang, P. Shape Control of Colloidal Metal Nanocrystals. *Small* **4**, 310-325 (2008).

20. Salehi-Khojin, A., Jhong, H. R. M., Rosen, B. A., Zhu, W., Ma, S., Kenis, P. J. & Masel, R. I. Nanoparticle Silver Catalysts that Show Enhanced Activity for Carbon Dioxide Electrolysis. *J. Phys. Chem. C* **117**, 1627-1632 (2013).

21. Arán Ais, R. M., Gao, D. & Roldan Cuenya, B. Structure- and Electrolyte-Sensitivity in CO_2 Electroreduction. *Acc. Chem. Res.* **51**, 2906-2917 (2018).

22. He, J., Johnson, N. J., Huang, A. & Berlinguette, C. P. Electrocatalytic Alloys for CO_2 Reduction. *ChemSusChem* **11**, 48-57 (2018).

23. Back, S., Yeom, M. S. & Jung, Y. Active Sites of Au and Ag Nanoparticle Catalysts for CO_2 Electroreduction to CO. *ACS Catal.* **5**, 5089-5096 (2015).

24. Liu, S., Tao, H., Zeng, L., Liu, Q., Xu, Z., Liu, Q. & Luo, J. L. Shape-Dependent Electrocatalytic Reduction of CO_2 to CO on Triangular Silver Nanoplates. *J. Am. Chem. Soc.* **139**, 2160-2163 (2017).

25. Bastys, V., Pastoriza Santos, I., Rodríguez González, B., Vaisnoras, R. & Liz Marzán, L. M. Formation of Silver Nanoprisms with Surface Plasmons at Communication Wavelengths. *Adv. Funct. Mater.* **16**, 766-773 (2006).

26. Kuhl, K. P., Hatsukade, T., Cave, E. R., Abram, D. N., Kibsgaard, J. & Jaramillo, T. F. Electrocatalytic Conversion of Carbon Dioxide to Methane and Methanol on Transition Metal Surfaces. *J. Am. Chem. Soc.* **136**, 14107-14113 (2014).

27. Barlow, J. M. & Yang, J. Y. Thermodynamic Considerations for Optimizing Selective CO_2 Reduction by Molecular Catalysts. *ACS Cent. Sci.* **5**, 580-588 (2019).

28. Li, Y. & Sun, Q. Recent Advances in Breaking Scaling Relations for Effective Electrochemical Conversion of CO_2. *Adv. Energy Mater.* **6**, 1600463 (2016).

29. Hong, X., Chan, K., Tsai, C. & Nørskov, J. K. How Doped MoS_2 Breaks Transition-Metal Scaling Relations for CO_2 Electrochemical Reduction. *ACS Catal.* **6**, 4428-4437 (2016).

30. Chan, K., Tsai, C., Hansen, H. A. & Nørskov, J. K. Molybdenum Sulfides and Selenides as Possible Electrocatalysts for CO_2 Reduction. *ChemCatChem* **6**, 1899-1905 (2014).

31. Zhu, W. L., Zhang, Y. J., Zhang, H. Y., Lv, H. F., Li, Q., Michalsky, R., Peterson, A. A. & Sun, S. S. Active and Selective Conversion of CO_2 to CO on Ultrathin Au Nanowires. *J. Am. Chem. Soc.* **136**, 16132-16135 (2014).

32. Li, F. & Tang, Q. Understanding the Role of Functional Groups of Thiolate Ligands in Electrochemical CO_2 Reduction over Au (111) from First-Principles. *J. Mater. Chem. A* **7**, 19872-19880 (2019).

33. Hoshi, N., Kato, M. & Hori, Y. Electrochemical Reduction of CO_2 on Single Crystal Electrodes of Silver Ag (111), Ag (100) and Ag (110). *J Electroanal. Chem.* **440**, 283-286 (1997).

34. Clark, E. L., Ringe, S., Tang, M., Walton, A., Hahn, C., Jaramillo, T. F., Chan, K. & Bell, A. T. Influence of Atomic Surface Structure on the Activity of Ag for the Electrochemical Reduction of CO_2 to CO. *ACS Catal.* **9**, 4006-4014 (2019).

35. Xu, R., Du, L., Adekoya, D., Zhang, G., Zhang, S., Sun, S. & Lei, Y. Well-Defined Nanostructures for Electrochemical Energy Conversion and Storage. *Adv. Energy Mater.* **2020**, 2001537 (2020).

36. Lauritsen, J. V., Kibsgaard, J., Helveg, S., Topsøe, H., Clausen, B. S., Lægsgaard, E. & Besenbacher, F. Size-Dependent Structure of MoS_2 Nanocrystals. *Nat. Nanotechnol.* **2**, 53-58 (2007).

37. Liu, X., Li, L., Yang, Y., Yin, Y. & Gao, C. One-Step Growth of Ttriangular Silver Nanoplates with Predictable Sizes on a Large Scale. *Nanoscale* **6**, 4513-4516 (2014).

38. Gobre, V. V. & Tkatchenko, A. Scaling Laws for van der Waals Interactions in Nanostructured Materials. *Nat. Commun.* **4**, 1-6 (2013).

39. Zeng, J., Roberts, S. & Xia, Y. Nanocrystal-Based Time-Temperature Indicators. *Chem. Eur. J.* **16**, 12559-12563 (2010).

40. Bae, Y., Kim, N. H., Kim, M., Lee, K. Y. & Han, S. W. Anisotropic Assembly of Ag Nanoprisms. *J. Am. Chem. Soc.* **130**, 5432-5433 (2008).

41. Qi, K., Cui, X. Q., Gu, L., Yu, S. S., Fan, X. F., Luo, M. C., Xu, S., Li, N. B., Zheng, L. R., Zhang, Q. H., Ma, J. Y., Gong, Y., Lv, F., Wang, K., Huang, H. H., Zhang, W., Guo, S. J., Zheng, W. T. & Liu, P. Single-Atom Cobalt Array Bound to Distorted 1T MoS_2 with Ensemble Effect for Hydrogen Evolution Catalysis. *Nat. Commun.* **10**, 1-9 (2019).

42. Naresh, N., Wasim, F. G. S., Ladewig, B. P. & Neergat, M. Removal of Surfactant and Capping Agent from Pd Nanocubes (Pd-NCs) Using *Tert*-Butylamine: Its Effect on Electrochemical Characteristics. *J. Mater. Chem. A* **1**, 8553-8559 (2013).

43. Liu, S., Wang, X. Z., Tao, H. B., Li, T. F., Liu, Q., Xu, Z. H., Fu, X. Z. & Luo, J. L. Ultrathin 5-Fold Twinned Sub-25 nm Silver Nanowires Enable Highly Selective Electroreduction of CO_2 to CO. *Nano Energy* **45**, 456-462 (2018).

44. De Luna, P., Quintero-Bermudez, R., Dinh, C. T., Ross, M. B., Bushuyev, O. S., Todorović, P., Regier, T., Kelley, S. O., Yang, P. D. & Sargent, E. H. Catalyst Electro-Redeposition Controls Morphology and Oxidation State for Selective Carbon Dioxide Reduction. *Nat. Catal.* **1**, 103-110 (2018).

45. Shan, C., Martin, E. T., Peters, D. G. & Zaleski, J. M. Site-Selective Growth of AgPd Nanodendrite-Modified Au Nanoprisms: High Electrocatalytic Performance for CO_2 Reduction. *Chem. Mater.* **29**, 6030-6043 (2017).

46. Trindell, J. A., Clausmeyer, J. & Crooks, R. M. Size Stability and H_2/CO Selectivity for Au Nanoparticles During Electrocatalytic CO_2 Reduction. *J. Am. Chem. Soc.* **139**, 16161-16167 (2017).

47. Sawyer, D. T., Sobkowiak, A. & Roberts, J. L. *Electrochemistry for Chemists*. (Wiley, 1995).

48. Jaramillo, T. F., Jørgensen, K. P., Bonde, J., Nielsen, J. H., Horch, S. & Chorkendorff, I. Identification of Active Edge Sites for Electrochemical H_2 Evolution from MoS_2 Nanocatalysts. *Science* **317**, 100-102 (2007).

49. Liu, S., Yang, H. B., Huang, X., Liu, L. H., Cai, W. Z., Gao, J. J., Li, X. N., Zhang, T., Huang, Y. Q. & Liu, B. Identifying Active Sites of Nitrogen-Doped Carbon Materials for the CO_2 Reduction Reaction. *Adv. Funct. Mater.* **28**, 1800499 (2018).

50. Yang, Y., Zhong, X. L., Zhang, Q., Blackstad, L. G., Fu, Z. W., Li, Z. Y. & Qin, D. The Role of Etching in the Formation of Ag Nanoplates with Straight, Curved and Wavy Edges and Comparison of Their SERS Properties. *Small* **10**, 1430-1437 (2014).

51. Hur, T. U. & Chung, W. S. Mechanism of Silver (I) Oxide Formation on Polycrystalline Silver Electrodes in 8 m KOH Solution. *J. Electrochem. Soc.* **152**, A179 (2004).

52. Pan, F. Zhang, H. G., Liu, K. X., Cullen, D., More, K., Wang, M. Y., Feng, Z. X., Wang, G. F., Wu, G. & Li, Y. Unveiling Active Sites of CO_2 Reduction on Nitrogen-Coordinated and Atomically Dispersed Iron and Cobalt Catalysts. *ACS Catal.* **8**, 3116-3122 (2018).

53. Abbasi, P., Asadi, M., Liu, C., Sharifi-Asl, S., Sayahpour, B., Behranginia, A., Zapol, P., Shahbazian-Yassar, R., Curtiss, L. A. & Salehi-Khojin, A. Tailoring the Edge Structure of

Molybdenum Disulfide toward Electrocatalytic Reduction of Carbon Dioxide. *ACS Nano* **11**, 453-460 (2017).

54. Asadi, M., Kim, K., Liu, C., Addepalli, A. V., Abbasi, P., Yasaei, P., Phillips, P., Behranginia, A., Cerrato, J. M., Haasch, R., Zapol, P., Kumar, B., Klie, R. F., Abiade, J., Curtiss, L. A. & Salehi-Khojin, A. Nanostructured Transition Metal Dichalcogenide Electrocatalysts for CO_2 Reduction in Ionic Liquid. *Science* **353**, 467-470 (2016).

55. Tao, H. C., Sun, X. F., Back, S., Han, Z. S., Zhu, Q. G., Robertson, A. W., Ma, T., Fan, Q., Han, B. X., Jung, Y. S. & Sun, Z. Y. Doping Palladium with Tellurium for the Highly Selective Electrocatalytic Reduction of Aqueous CO_2 to CO. *Chem. Sci.* **9**, 483-487 (2018).

56. Zhao, H. C., Sun, X. F., Back, S., Han, Z. S., Zhu, Q. G., Robertson, A. W., Ma, T., Fan, Q., Han, B. X., Jung, Y. S. & Sun, Z. Y. Ionic Exchange of Metal-Organic Frameworks to Access Single Nickel Sites for Efficient Electroreduction of CO_2. *J. Am. Chem. Soc.* **139**, 8078-8081 (2017).

57. Zhang, X., Wu, Z. S., Zhang, X., Li, L. W., Li, Y. Y., Xu, H. M., Li, X. X., Yu, X. L., Zhang, Z. S., Liang, Y. Y. & Wang, H. L. Highly Selective and Active CO_2 Reduction Electrocatalysts Based on Cobalt Phthalocyanine/Carbon Nanotube Hybrid Structures. *Nat. Commun.* **8**, 1-8 (2017).

58. Kramer, W. & McCrory, C. Polymer Coordination Promotes Selective CO_2 Reduction by Cobalt Phthalocyanine. *Chem. Sci.* **7**, 2506-2515 (2016).

59. Zhang, B. X., Zhang, J. L., Shi, J. B., Tan, D. X., Liu, L. F., Zhang, F. Y., Lu, C., Su, Z. Z., Tan, X. N., Cheng, X. Y., Han, B. X., Zheng, L. R. & Zhang, J. Manganese Acting as a High-

Performance Heterogeneous Electrocatalyst in Carbon Dioxide Reduction. *Nat. Commun.* **10**, 1-8 (2019).

60. Sun, X. F., Chen, C. J., Liu, S. J., Hong, S., Zhu, Q. G., Qian, Q. L., Han, B. X., Zhang, J. & Zheng, L. R. Aqueous CO_2 Reduction with High Efficiency Using α-Co $(OH)_2$-Supported Atomic Ir Electrocatalysts. *Angew. Chem. Int. Ed.* **58**, 4669-4673 (2019).

61. Wang, X. Q., Chen, Z., Zhao, X. Y., Yao, T., Chen, W. X., You, R., Zhao, C. M., Wu, G., Wang, J., Huang, W. X., Yang, J. L., Hong, X., Wei, S. Q., Wu, Y. & Li, Y. D. Regulation of Coordination Number over Single Co Sites: Triggering the Efficient Electroreduction of CO_2. *Angew. Chem. Int. Ed.* **57**, 1944-1948 (2018).

62. Gu, J., Hsu, C. S., Bai, L., Chen, H. M. & Hu, X. Atomically Dispersed Fe^{3+} Sites Catalyze Efficient CO_2 Electroreduction to CO. *Science* **364**, 1091-1094 (2019).

63. Hsieh, Y. C., Senanayake, S. D., Zhang, Y., Xu, W. & Polyansky, D. E. Effect of Chloride Anions on the Synthesis and Enhanced Catalytic Activity of Silver Nanocoral Electrodes for CO_2 Electroreduction. *ACS Catal.* **5**, 5349-5356 (2015).

64. Sun, K., Wu, L. N., Q, W., Zhou, J. G., Hu, Y. F., Jiang, Z. H., Shen, B. Z. & Wang, Z. J. Enhanced Electrochemical Reduction of CO_2 to CO on Ag Electrocatalysts with Increased Unoccupied Density of States. *J. Mater. Chem. A* **4**, 12616-12623 (2016).

65. Ihida, M., Kikkawa, S., Hori, K., Teramura, K., Asakura, H., Hosokawa, S. & Tanaka, T. Effect of Surface Reforming *via* O_3 Treatment on the Electrochemical CO_2 Reduction Activity of a Ag Cathode. *ACS Appl. Energ. Mater.* **3**, 6552-6560 (2020).

66. Kibsgaard, J., Jaramillo, T. F. & Besenbacher, F. Building an Appropriate Active-Site Motif into a Hydrogen-Evolution Catalyst with Thiomolybdate $[Mo_3S_{13}]^{2-}$ Clusters. *Nat. Chem.* **6**, 248 (2014).

67. Kresse, G. & Hafner, J. *Ab initio* Molecular Dynamics for Liquid Metals. *Physical Review B* **47**, 558 (1993).

68. Kresse, G. & Hafner, J. *Ab initio* Molecular Dynamics for Open-Shell Transition Metals. *Physical Review B* **48**, 13115 (1993).

69. Perdew, J. P., Burke, K. & Ernzerhof, M. Generalized Gradient Approximation Made Simple. *Phys. Rev. Lett.* **77**, 3865 (1996).

SYNOPSIS. If you are submitting your paper to a journal that requires a synopsis, see the journal's Instructions for Authors for details.